View Online / Journal Homepage / Table of Contents for this issue
Dynamic Article Links

Energy &
Environmental Science

Cite this: *Energy Environ. Sci.*, 2011, **4**, 4954

www.rsc.org/ees

PAPER

A general strategy toward graphene@metal oxide core–shell nanostructures for high-performance lithium storage†

Weiwei Zhou,[a] Jixin Zhu,[b] Chuanwei Cheng,[a] Jinping Liu,[ac] Huanping Yang,[a] Chunxiao Cong,[a] Cao Guan,[a] Xingtao Jia,[a] Hong Jin Fan,[a] Qingyu Yan,[b] Chang Ming Li[d] and Ting Yu*[ae]

Received 18th July 2011, Accepted 9th August 2011
DOI: 10.1039/c1ee02168k

We demonstrate a simple, efficient, yet versatile method for the realization of core–shell assembly of graphene around various metal oxide (MO) nanostructures, including nanowires (NWs) and nanoparticles (NPs). The process is driven by (i) the ring-opening reaction between the epoxy groups and amine groups in graphene oxide (GO) platelets and amine-modified MO nanostructures, respectively, and (ii) electrostatic interaction between these two components. Nearly every single NW or NP is observed to be wrapped by graphene. To the best of our knowledge, this is the first report that substrate-supported MO NWs are fully coated with a graphene shell. As an example of the functional properties of these compound materials, the graphene@α-Fe_2O_3 core–shell NPs are investigated as the lithium-ion battery (LIB) electrode, which show a high reversible capacity, improved cycling stability, and excellent rate capability with respect to the pristine α-Fe_2O_3. The superior performance of the composite electrode is presumably attributed to the effectiveness of the graphene shell in preventing the aggregation, buffering the volume change, maintaining the integrity of NPs, as well as improving the conductivity of the electrode.

Introduction

Engineering of hybrid nanostructures has attracted tremendous attention due to its diverse functionalities integrated in a single object.[1] Graphene is an up-and-coming carbon material comprised of monolayered hexagonal sp^2 hybridized carbons. Together with atomic thickness, the two-dimensional conjugated chemical structure endows graphene with a host of attractive properties, such as large specific surface area, excellent electrical conductivity, good mechanical flexibility and strong thermal/chemical stability.[2] It thus has been considered as an ideal reinforcing component for hybrids

Broader context

The impending exhaustion of fossil fuels and the rising global demand for energy require society to move towards sustainable energy production, storage, and consumption. As an important part, the advances of energy storage techniques strongly depend on the achievements of material science. Graphene is an emerging carbon material consisting of monolayered sp^2 hybrid carbon atoms and possesses large specific surface area, excellent electrical conductivity, good mechanical flexibility, and strong thermal/chemical stability. Such a synergistic combination of attractive properties renders graphene a promising component for energy storage devices. During the past several years, various graphene based materials, especially graphene/metal oxide (MO) composites, have been successfully prepared and applied in supercapacitors and lithium ion batteries (LIBs). Here, we demonstrate a simple, efficient, yet versatile method for the realization of core–shell assembly of graphene around different MO nanostructures, including nanowires (NWs) and nanoparticles (NPs). Nearly every single NW or NP is observed to be wrapped by graphene. In comparison with pristine MO, the graphene@MO core–shell nanostructure shows significantly improved reversible capacity, cycling stability, and rate capability when applied as an electrode for LIBs. This work is probably of wide interest to those who work on graphene/MO composites for energy storage devices.

---

[a] *Division of Physics and Applied Physics, School of Physical and Mathematical Sciences, Nanyang Technological University, 21 Nanyang Link, 637371, Singapore. E-mail: yuting@ntu.edu.sg*
[b] *School of Materials Science and Engineering, Nanyang Technological University, 50 Nanyang Avenue, Singapore, 639798, Singapore*
[c] *Institute of Nanoscience and Nanotechnology, Department of Physics, Central China Normal University, Wuhan, 430079, P.R. China*
[d] *School of Chemical and Biomedical Engineering, Nanyang Technological University, 70 Nanyang Drive, 637457, Singapore*
[e] *Department of Physics, Faculty of Science, National University of Singapore, 117542, Singapore*

† Electronic supplementary information (ESI) available. See DOI: 10.1039/c1ee02168k

or composites. Hitherto, graphene has been blended with various organic and inorganic components to form functional composites.[3] The incorporation of graphene into the composites can provide them with the unique functions of graphene and also possibly induce intriguing properties inherited from the synergetic effect. As a result, various graphene-based hybrid nanostructures have emerged in diverse areas such as catalysis,[4] sensors,[5] optoelectronics,[6] and energy conversion and storage devices.[7]

Of these, the lithium-ion battery (LIB) indeed benefits greatly from the introduction of graphene as a component of its electrode.[7b,8] It is known that transition metal oxides (MOs), albeit regarded as promising anode materials with high theoretical capacity (~500 to 1000 mA h g^{-1}, compared with 372 mA h g^{-1} for conventional graphite), still suffer from the problems of poor electrical conductivity and unsatisfactory cycling stability. The emergence of graphene provides new hope to alleviate these problems. A variety of transition MOs have been coupled with graphene and, as expected, demonstrated superior electrochemical performance.[8a,9] In general, graphene sheets (GS) in the as-obtained composites can (1) function as conductive channels; (2) provide an elastic buffer space to accommodate the volume change during repeated lithium uptake and removal reactions; and (3) prevent the aggregation of MO nanoparticles (NPs) and the cracking or crumbling of electrode material upon cycling.[8a,10] Consequently, the conductivity and integrity of the composite electrode can be effectively improved compared with the pristine MO electrode. Although tremendous efforts have been devoted to coupling graphene with MOs, current research accomplishments are mainly focused on graphene/MO NP composites;[8c,9b,9c,10,11] there are few reports on integrating one dimensional (1D) nanostructure with graphene,[12] in spite of its promising applications especially in energy storage and conversion devices. Furthermore, a versatile method for coupling graphene with MO nanostructures of different dimensions is lacking.

Herein, we describe a simple and general strategy to wrap graphene onto different MO nanostructures including nanowires (NWs) and NPs. The fabrication procedure consists of three steps: pre-modification of MOs with amine groups, coating of a graphene oxide (GO) layer, and finally conversion of the GO shell to graphene. Of note, all steps are accomplished by simply immersing the pre-grown MO nanostructures into corresponding functional solutions at room temperature. Strikingly, the GS wrapping occurs along the entire length of individual MO NWs and the main body of every MO NPs. As a proof-of-concept demonstration of the application of such graphene-based core–shell nanostructures, graphene-wrapped α-Fe_2O_3 NPs are tested as the LIB anode. Compared with pristine α-Fe_2O_3, significantly improved specific capacity, rate capability, and cycling stability have been demonstrated. This can be attributed to the enhanced electron transport efficiency and structural integrity of the NPs arising from the graphene encapsulation.

Experimental

1. GO preparation

GO was prepared by a modified Hummers method.[13] Firstly, 2 g of graphite powder and 1.5 g of $NaNO_3$ were added into 150 mL of 98% H_2SO_4 solution in a flask immersed in an ice bath. With the stirring still in progress, 9 g of $KMnO_4$ was added slowly, little by little, to the mixture to prevent a sudden accumulation of heat that is evolved. After that the mixture was stirred for 5 days at room temperature. Then, 10 mL of 30% H_2O_2 was added into the solution in order to completely react with the remaining $KMnO_4$, leading to a bright yellow solution. To purify the graphene oxide, the resulting mixture was washed by 3% H_2SO_4 and H_2O until the pH value of the solution was approximately 5–6. GO powder was obtained after freeze drying the suspension.

2. Synthesis of graphene@metal oxide core–shell nanostructures

2.1 Synthesis of SnO_2, CuO, and CoO NWs. The SnO_2 NWs on a stainless steel (SS) substrate and oriented CuO NWs on a copper substrate were prepared *via* a standard chemical-vapor-deposition (CVD) method[1a] and a simple vapour–solid reaction method,[14] respectively, according to our previous work. CoO NWs on Ti foil were also prepared through a two-step method reported previously.[15]

2.2 Synthesis of α-Fe_2O_3 NPs. Different from the above approaches, the method for synthesizing α-Fe_2O_3 NPs is firstly reported here. In a typical procedure, 0.417 g of $FeSO_4 \cdot 7H_2O$ and 0.4 g of sodium citrate were dissolved in 30 mL of distilled water. After complete dissolution, the mixture was sealed into a Teflon-lined autoclave and maintained at 180 °C for 8 h. After it was cooled down to room temperature, the precipitation was collected and washed with distilled water and ethanol. The α-Fe_2O_3 NPs were obtained by annealing the as-collected precursor at 450 °C for 2 h in air.

2.3 Preparation of graphene@metal oxide nanostructures. Wrapping GS onto the surfaces of MO nanostructures was achieved by immersing the pre-formed MOs sequentially into the following three solutions for varied durations at room temperature.

(I) Poly(allylamine hydrochloride) (PAH) solution (1 g L^{-1}), 1 h.
(II) GO dispersion (0.2 g L^{-1}), 5 h.
(III) Hydrazine (N_2H_4, 98%) 0.5 h.

For NW samples, all these steps can be accomplished by simply dipping the pre-grown substrate-supported MO NWs into corresponding solutions. While for α-Fe_2O_3 NPs, each step needs to be assisted with magnetic stirring to ensure a homogeneous mixture and centrifugation to separate the NPs.

3. Characterization

Powder X-ray diffraction (XRD) analysis was performed using a D8 Advanced diffractometer with Cu Kα line. Transmission electron microscopy (TEM) images were recorded by a JEOL JEM-2010 transmission electron microscope with an accelerating voltage of 200 kV. Field-emission scanning electron microscopy (FESEM) analysis was conducted with a JEOL JSM-6700F electron microscope. Raman spectra and images were obtained by a WITeck CRM200 confocal microscopy Raman system with a piezocrystal controlled scanning stage. The excitation light is a 532 nm laser. The laser spot size is estimated to be 500 nm. Atomic force microscopy (AFM) was carried out using a Digital

Nanoscope V in the tapping mode. An etched silicon tip was used as a probe for imaging the samples. Thermogravimetry analyses (TGA, Q500) were carried out in the temperature range of 40 to 700 °C at a heating rate of 10 °C min^{-1} in air. The surface area of graphene@α-Fe_2O_3 NPs was measured using Brunauer–Emmett–Teller (BET) (Quantachrome Instruments, Autosorb AS-6B). The Fourier-transformed infrared (FT-IR) spectroscopy was measured using the KBr-pellet method in transmission mode on a NEXUS 670 FT-IR spectrometer.

4. Electrochemical measurement

The graphene@α-Fe_2O_3 and pristine α-Fe_2O_3 NPs were dried at 150 °C for 30 min under Ar atmosphere. Then, 80 wt% active material (graphene/α-Fe_2O_3 or α-Fe_2O_3), 10 wt% acetylene black (Super-P), and 10 wt% polyvinylidene fluoride (PVDF) binder were mixed into *N*-methyl-2-pyrrolidinone (NMP). The obtained slurry was coated onto Cu foil disks to form working electrodes, which were then dried in vacuum at 50 °C for 12 h to remove the solvent. Electrochemical measurements were performed using two-electrode CR2032 (3 V) coin-type cells with lithium foil serving as both counter and reference electrodes under ambient temperature. The electrolyte was 1 M $LiPF_6$ in a 50 : 50 (w/w) mixture of ethylene carbonate (EC) and dimethyl carbonate (DMC). Cell assembly was carried out in an argon-filled glovebox with both moisture and oxygen contents below 1.0 ppm. Galvanostatic charge/discharge tests were performed using a NEWARE battery tester at a voltage window of 0.005–3 V. Cyclic voltammetry (CV, 0.005–3 V, 0.5 mV s^{-1}) was performed using an electrochemical workstation (CHI 760D).

Results and discussion

I Wrapping graphene on MO NWs

Fig. 1 shows a typical preparation route and the proposed formation mechanism of the graphene@MO core–shell NWs. To achieve the coating of GS, pre-synthesized MO NWs are just dipped sequentially into poly(allylamine hydrochloride) (PAH) solution, GO dispersion, and hydrazine (N_2H_4) solution for 1 h, 5 h, and 0.5 h, respectively (Fig. 1a). PAH solution here is used to modify the MO NWs by grafting onto their surface, providing them with amine end groups. Subsequent impregnation into GO dispersion makes the GO platelets spontaneously assemble onto the surface of PAH-modified MO NWs. This process occurs likely through two interactions: (i) the ring-opening reaction between the amine groups in the functionalized MO NWs and the epoxy groups in the GO platelets;[3b,16] and (2) electrostatic interaction between the positively charged amine-modified MO NWs and negatively charged GO platelets.[3a,9c] Abundant amine groups in the PAH-modified NWs are able to cross-link the GO platelets *via* the epoxy groups of two or more platelets, stitching them together (Fig. 1b).[16b] In conjunction with the electrostatic interaction, such a chemical cross-linking results eventually in the marvellous core–shell assembly between the NWs and GO platelets. The resulting GO@MO NWs are then subjected to the N_2H_4 solution aiming at transforming GO into graphene (Fig. 1c). As shown in the scheme, in addition to the ones wrapped on the surface of the NWs, there should also be some GO platelets (and subsequent GS) stretching across the NWs (indicated by the red dashed arrows).

Three typical MO NWs, namely, SnO_2, CuO, and CoO NWs, are adopted to verify the feasibility and versatility of our protocol in achieving graphene@MO core–shell NWs. Corresponding XRD patterns of these NWs are shown in Fig. S1†. The thickness of the GO platelet in the dispersion is measured to be ~1 nm, indicating the monolayered structure (Fig. S2†).[17] We firstly test this concept with the SnO_2 NWs grown on stainless steel (SS) substrates *via* a CVD method. No obvious change is noticed before and after GS coating under low-magnification scanning electron microscope (SEM) observation (Fig. S3a and b†). However, Raman characterization indeed manifests the presence of GO and graphene at corresponding steps (Fig. S3c†). Fig. 2a displays a representative SEM image of the graphene@SnO_2 NWs. At first glance, the SnO_2 NWs are just randomly interspersed rather than discernibly coated with GS (indicated by the red dashed circles). The strong Raman signals of the D and G bands of graphitic material were thus initially thought to stem from these randomly distributed GS (inset in Fig. 2a). However, careful observation enables us to grab a clear view of the core–shell structure (Fig. 2b). Another interesting observation of the graphene shell tearing up from one end of a SnO_2 NW reveals that GS are indeed tightly attached onto the SnO_2 NWs (Fig. 2c). A high-magnification transmission electron microscope (TEM) image further reveals the core–shell structure (Fig. 2d). The thickness of the graphene shell is approximately in the range from 1 to 3 nm (Fig. 2d). More straightforward evidence of the complete graphene wrapping around the NWs is imparted by the Raman mapping results of the D and G bands of graphene for randomly chosen single NWs (Fig. 2e and f, and S4†).

CuO NWs obtained from directly heating the copper foil in air represent another type of NWs following the vapour–solid growth mechanism. Unlike the case for SnO_2 NWs, after a series of immersions in different solutions, the tips of CuO NWs are prone to bind together due primarily to the capillary force (Fig. 3a and b). Further inspection under high-magnification SEM shows the presence of GS intertwining between the CuO NWs (Fig. 3c). Although the core–shell structure is not easily discernible under SEM (Fig. 3d and e), TEM observation can still identify the continuous graphene shell (Fig. 3f). The complete coverage of the GS is evidenced by Raman mapping of different single graphene@CuO NWs as well (Fig. 3g and h, and S5†). Apart from solid SnO_2 and CuO NWs, porous CoO NWs on Ti foil *via* thermal-decomposition are adopted to further prove the applicability of our method to porous NWs. The results resemble the cases for SnO_2 and CuO NWs, revealing the core–shell structure and continuous GS coating along entire individual NW (Fig. S6†).

II Wrapping graphene on MO NPs

In addition to MO NWs, this strategy can also be easily extended to MO NPs. Here, α-Fe_2O_3 NPs obtained from thermal-decomposition of a Fe-containing precursor are employed to demonstrate the efficiency and adaptability of this approach. It can be seen that the precursor NPs are composed of sub-nanoparticles and are fairly uniform in size and shape with diameters of around 150 nm (Fig. 4a–c). Remarkably, these precursor NPs are stacked in a highly ordered way (Fig. S7†), which arises

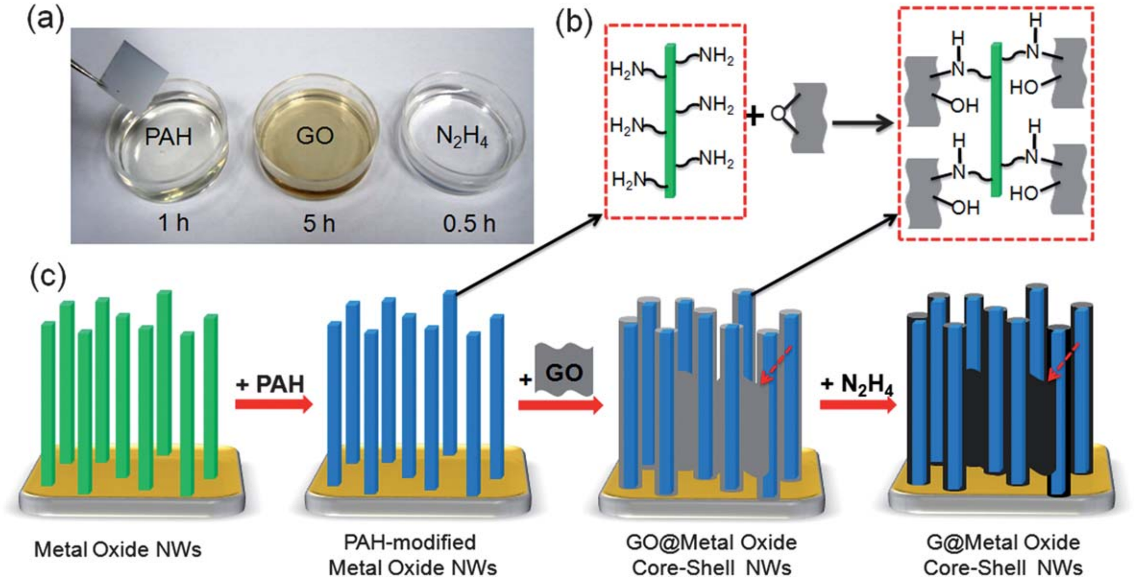

Fig. 1 (a) Optical image of the solutions used in our dipping method; the sample held by the tweezer is SnO_2 NWs on stainless steel substrate. (b) The proposed ring-opening reaction mechanism between the amine groups in the PAH-functionalized MO NWs and the epoxy groups in the GO sheets. (c) Schematic illustration of the fabrication process for graphene@MO core–shell NWs. Red dashed arrows indicate the GO and graphene sheets stretching across the NWs.

possibly from the self-assembly process of sub-nanoparticles. As the reaction system is free of any surfactants and other organic molecules, the citrate ligands are believed to act as the stabilizer of such a self-assembled structure. After annealing, the Fe-containing precursors are transformed to α-Fe_2O_3 with "rose-like" morphology (Fig. 4d and e and S8†). Despite the phase and shape transitions, the resulting α-Fe_2O_3 "nano-roses" still show high uniformity (Fig. S9†). However, the highly ordered stacking mode is destroyed probably due to the decomposition of citrate ligands. TEM characterization further discloses the porous structure of these α-Fe_2O_3 "nano-roses", which is likely caused by the removal of CO_2, CO, and H_2O gases and lattice contraction during annealing (Fig. 4f). Following the same procedures for wrapping graphene on MO NWs but conducted in beakers aided by magnetic stirring, GS can also be successfully wrapped around the surfaces of α-Fe_2O_3 "nano-roses" (Fig. 4g–i). The Fourier-transformed infrared (FT-IR) spectra show that the epoxy C–O stretch at 1220 cm^{-1} presented in GO

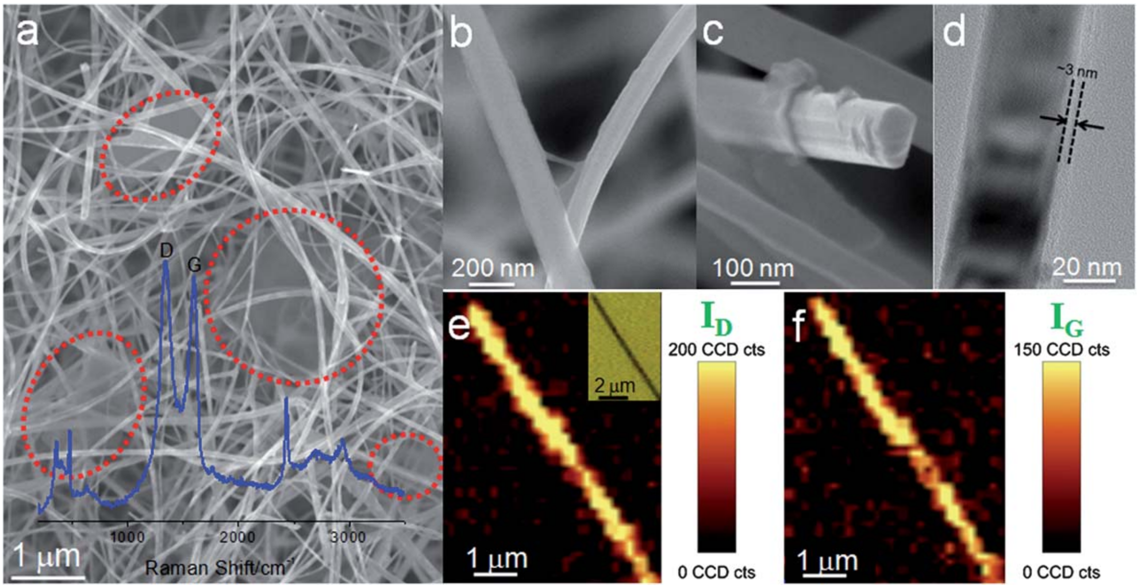

Fig. 2 (a) Low-magnification and (b and c) high-magnification SEM images of graphene@SnO_2 NWs. The inset in (a) is the Raman spectrum taken from those graphene@SnO_2 NWs. (d) TEM image of a single graphene@SnO_2 NW. (e and f) Raman mapping images of the D and G bands of graphene for a single graphene@SnO_2 NW. The inset in (e) shows the optical image of the selected NW.

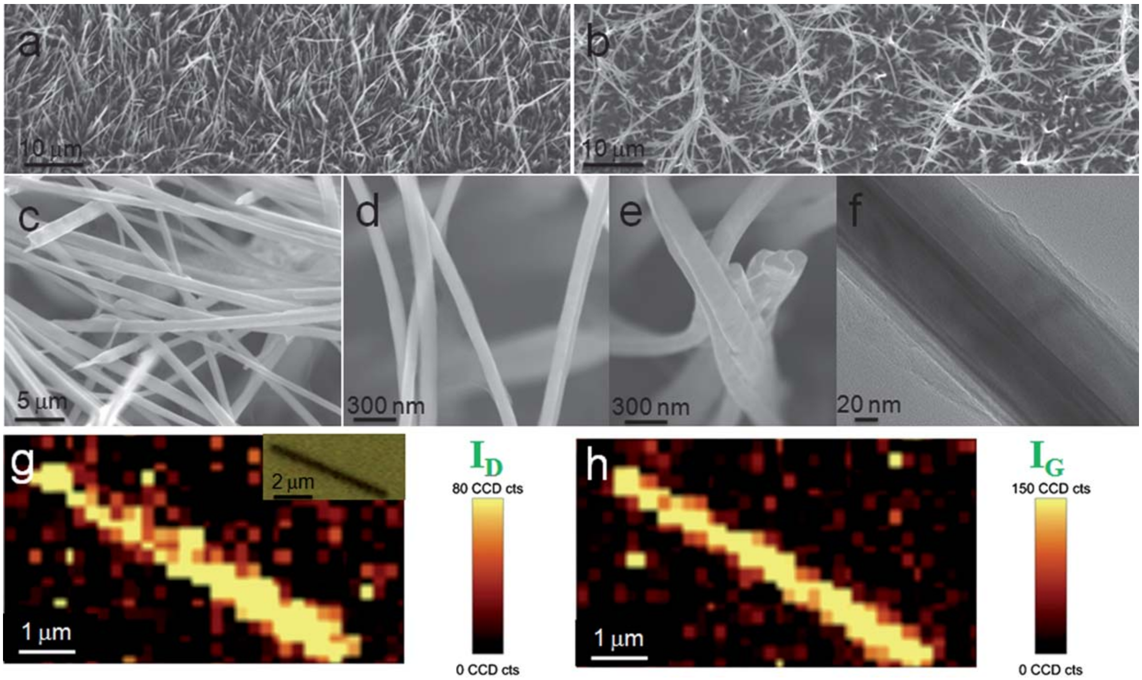

Fig. 3 Low-magnification SEM images of (a) CuO NWs and (b) graphene@CuO NWs. (c–e) High-magnification SEM images of graphene@CuO NWs. (d) High-magnification TEM image of a single graphene@CuO NW, revealing thick graphene coating. (g and h) Raman mapping images of the D and G bands of graphene for a single graphene@CuO NW. The inset in (g) shows the optical image of the selected NW.

disappeared for GO@α-Fe_2O_3, which is probably interpreted as evidence of the ring-opening reaction between the epoxy groups in GO and the amine groups in PAH-modified α-Fe_2O_3 NPs (see details in Fig. S10†).[16a] The resulting graphene-encapsulated α-Fe_2O_3 "nano-roses" (G@α-Fe_2O_3) exhibit crinkled and rough textures, which are associated with the presence of flexible and ultrathin GS. In addition to wrapping on individual NPs, in some cases GS appear to interconnect neighboring NPs (Fig. 4g–i). For quantifying the amount of graphene in the G@α-Fe_2O_3 composite, thermogravimetric analysis (TGA) was carried out in air. The result reveals that the weight fraction of graphene is as low as 2.8% (Fig. 5a), which is much lower than those of previously reported graphene/MO composites.[9c,11b,18] Herein, the weight loss at the temperature below 100 °C is attributed to the evaporation of moisture.[11b] Moreover, the nitrogen isotherm adsorption–desorption curve together with the pore size distribution of G@α-Fe_2O_3 is given in Fig. 5b, disclosing that the BET specific surface area is around 79.5 $m^2\ g^{-1}$ and the main pore size is about 20 nm.

III Electrochemical performance of G@α-Fe_2O_3 toward lithium storage

To demonstrate the effectiveness of the graphene-based compound nanostructure in improving the lithium storage performance, the electrochemical properties of G@α-Fe_2O_3 as the anode were

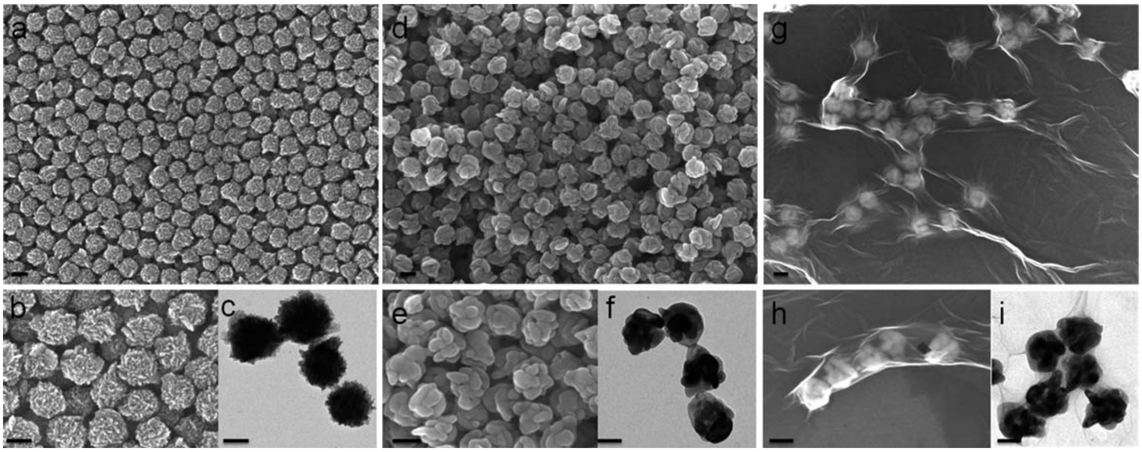

Fig. 4 (a) Low-magnification, (b) high-magnification SEM images, and (c) TEM image of the as-obtained α-Fe_2O_3 precursor; (d) low-magnification, (e) high-magnification SEM images, and (f) TEM image of the α-Fe_2O_3 NPs; (g) low-magnification, (h) high-magnification SEM images, and (i) TEM image of the as-prepared graphene@α-Fe_2O_3 NPs. All the scale bars in the figures and insets are 100 nm.

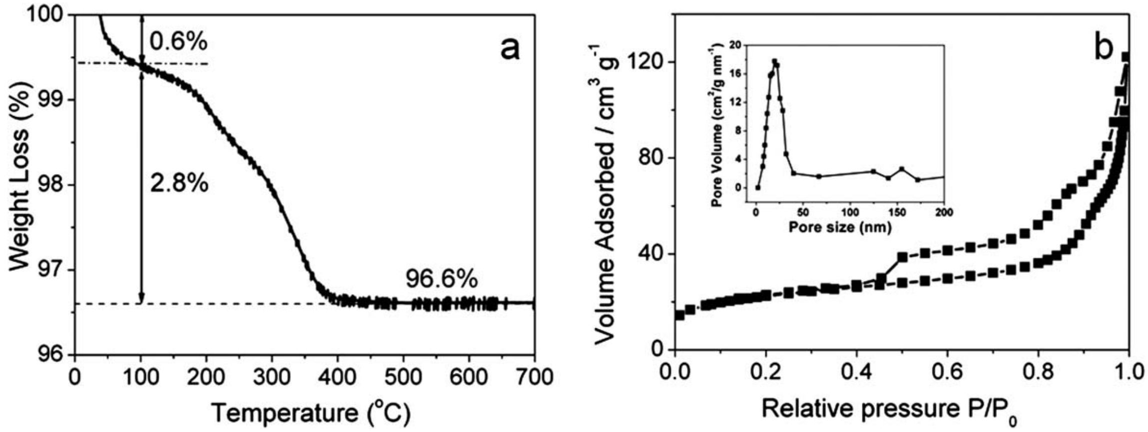

Fig. 5 (a) Thermogravimetric analysis of G@α-Fe_2O_3 NPs composite. (b) Nitrogen isotherm adsorption–desorption curve of G@α-Fe_2O_3 NPs. The inset shows their pore size distributions.

investigated by galvanostatic charge–discharge measurements. The voltage–capacity trace of pristine α-Fe_2O_3 NPs was also recorded for comparison. Fig. 6a displays the first discharge/charge voltage profiles of α-Fe_2O_3 and G@α-Fe_2O_3 electrodes in the voltage window of 0.005–3.0 V at a rate of 200 mA g^{-1} (C/5, 1 C is defined as 1007 mA g^{-1}), showing the well-known signature of conversion reactions of iron oxides.[11b,18,19] Specifically, the voltage decreases steeply to *ca.* 1.65 V, and then followed by a small slope (marked as 1). When the voltage continues to decrease to *ca.* 1.05 V, the second slope appears (marked as 2), which delivers a capacity of *ca.* 250 mA h g^{-1}. A long plateau is clearly observed when the voltage decreases to *ca.* 0.85 V (marked as 3), delivering a capacity of *ca.* 850 mA h g^{-1}. Thereafter, the voltage gradually decreases to the cut-off value. In general, the voltage slopes at *ca.* 1.65 V and 0.85 V are ascribed to the lithium intercalation and the reduction reaction of α-Fe_2O_3 to metallic Fe, respectively. Recently, the slope at *ca.* 1.05 V is attributed to the formation of an intermediate cubic phase $Li_2Fe_2O_3$.[19a,20] The above processes are summarized into the following three lithiation steps:

$$\alpha\text{-}Fe_2O_3 \rightarrow \alpha\text{-}Li_xFe_2O_3 \rightarrow \text{cubic } Li_2Fe_2O_3 \leftrightarrow Fe + Li_2O$$

While the electrochemical reaction pathways are the same, the cyclic performances of the G@α-Fe_2O_3 composite and pristine α-Fe_2O_3 are distinctly different (Fig. 6b). Apparently, the G@α-Fe_2O_3 composite delivers a much higher capacity than bare α-Fe_2O_3 throughout the cycling. In the first cycle, the discharge capacity of the α-Fe_2O_3 particle electrode is about 1179 mA h g^{-1}; the excess capacity compared with the theoretical value (~1007 mA h g^{-1}) seems to derive from electrolyte decomposition in the low-potential region and the subsequent formation of an organic layer on the surface of the particles.[8b] However, the capacity decreases to 290 mA h g^{-1} after 100 cycles with only about 25% retention. In contrast, the α-Fe_2O_3 NPs, after being wrapped by graphene, show much improved cycling stability. From the 48th cycle, the capacity of the G@α-Fe_2O_3 composite starts to increase and reaches ~781 mA h g^{-1} at the 100th cycle, which is much higher than that of bare α-Fe_2O_3 NPs. The initial discharge capacity is 1338 mA h g^{-1}; therefore 58% of the reversible capacity can be maintained over 100 cycles at a current density of 200 mA g^{-1}. One interesting phenomenon is that both electrodes exhibit an increasing trend of the capacity after certain cycles. This has also been observed in other transition-MO based cells and is possibly attributed to some long-term activation processes during charge–discharge cycling.[11b,21]

To better understand the advantage of the G@α-Fe_2O_3 composite in lithium storage, the discharge capacities under adjoining cycles of different rates were compared for both G@α-Fe_2O_3 and bare α-Fe_2O_3 electrodes (Fig. 6c). Note that, with respect to the reference α-Fe_2O_3, the specific capacity of G@α-Fe_2O_3 is substantially increased at all investigated charge–discharge rates from C/5 to 10 C. For example, the specific capacity of G@α-Fe_2O_3 at a rate of 5 C is as high as 269 mA h g^{-1}, 34 times higher than that of bare α-Fe_2O_3 (8 mA h g^{-1}). Moreover, the G@α-Fe_2O_3 electrode can still deliver a high capacity of 143 mA h g^{-1} at a rate of 10 C, whilst the bare α-Fe_2O_3 cannot store charges any more. Importantly, after the high rate measurements, the specific capacities of both electrodes at C/5 are able to recover to almost the initial values, implying their good reversibility.

The increased specific capacity, good cycling stability, and enhanced high-rate capability of the G@α-Fe_2O_3 composite are attributed to its unique structure. As can be seen from the above results, the composite electrode has a high weight fraction of electrochemically active α-Fe_2O_3, large specific surface area, and ultrathin graphene shells as both buffer matrix and conducting pathways, which are all crucial factors accounting for the superior electrochemical properties. The former two characteristics are propitious to reach high specific capacity of the G@α-Fe_2O_3 composite. It is well-known that one advantage of transition-metal oxides over carbon-based materials in lithium storage is their high theoretical specific capacity. Hence, a large content of α-Fe_2O_3 could give rise to a high specific capacity. The large specific surface area, obviously, is highly favourable for LIB to achieve high specific capacity as it can provide more electrochemically active sites for Li^+ insertion/extraction. In addition to these two features, the GS contribute more to the improved cycling stability and excellent rate capability for the following reasons. On one hand, the presence of GS can suppress the aggregation, buffer the volume change of α-Fe_2O_3 NPs, and maintain the electrical contact between α-Fe_2O_3 NPs and current

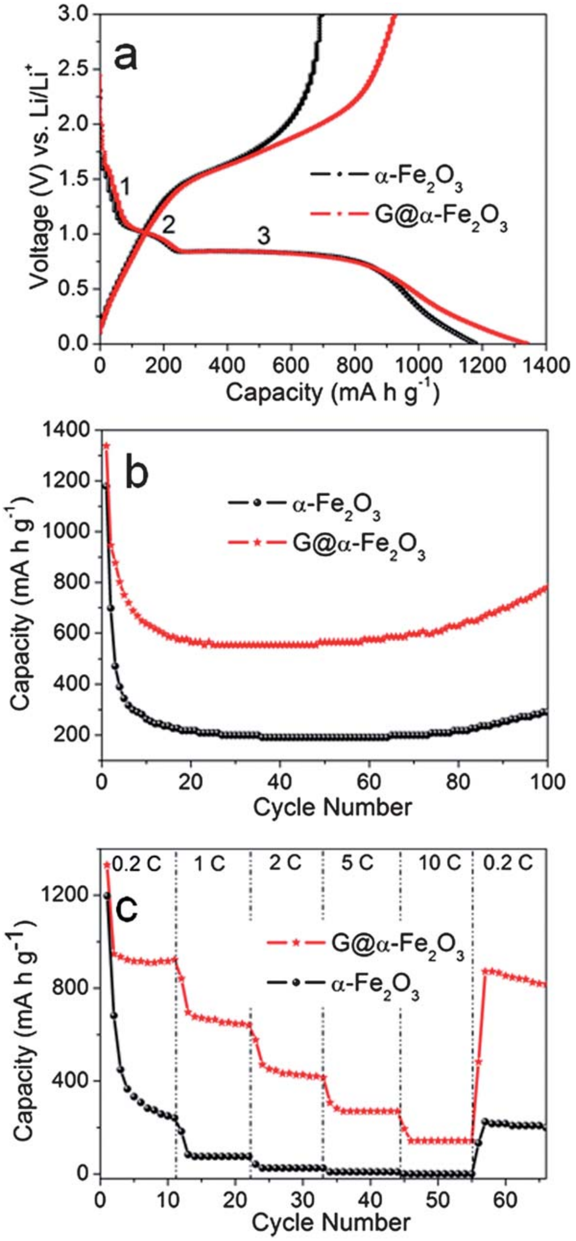

Fig. 6 (a) Voltage–capacity profiles of G@α-Fe_2O_3 composite and pristine α-Fe_2O_3 NPs for the first cycle at the current density of 200 mA g^{-1}. (b) Cycling performance of G@α-Fe_2O_3 composite and pristine α-Fe_2O_3 NPs at a current rate of C/5 (200 mA g^{-1}). (c) Cyclic stabilities of G@α-Fe_2O_3 composite and pristine α-Fe_2O_3 NPs at various rates.

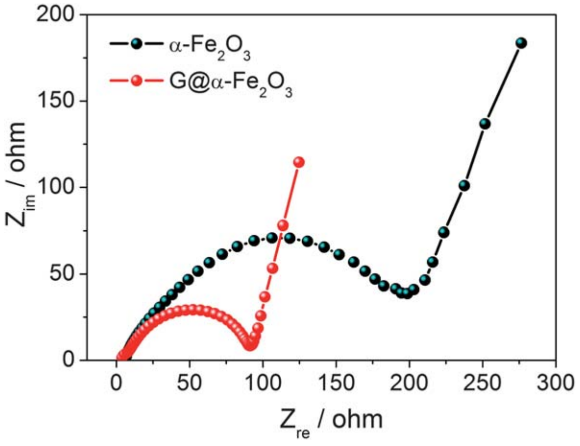

Fig. 7 Nyquist plots of the electrodes of G@α-Fe_2O_3 composite and pristine α-Fe_2O_3 NPs.

collector as well during the cycling, thereby resulting in better cyclic stability with respect to the bare α-Fe_2O_3 NPs. On the other hand, graphene can facilitate electron transfer from wrapped porous α-Fe_2O_3 NPs within the whole electrode. Compared with bare α-Fe_2O_3 NPs, the conductive GS matrix in the composite electrode can act as "highways" for electron transportation between α-Fe_2O_3 NPs, which decreases the inner resistance, thus leading to a better rate capability. It needs to be pointed out that the graphene shell obtained from chemical reduction of GO contains a lot of defects and can thereby access the Li^+ diffusion through these defective sites. To confirm the good conductivity of the composite electrode, Fig. 7 compares the Nyquist plots of G@α-Fe_2O_3 and α-Fe_2O_3 NPs. Apparently, the G@α-Fe_2O_3 electrode possesses a much lower resistance than the α-Fe_2O_3 electrode (~90 *vs.* ~199 Ω), thus suggesting that the composite electrode possesses lower contact and charge-transfer impedances.[9c] As a result, Li^+ diffusion and electron transfer are expedited at high cycling rates for the G@α-Fe_2O_3 electrode.

Conclusions

A general strategy is developed based on the ring-opening reaction between epoxy groups and amine groups and electrostatic interaction to achieve the self-assembled wrapping of graphene sheets around various metal oxide NWs and NPs. Raman mapping reveals the full coverage of an entire NW by graphene. The effectiveness of the graphene shell in preventing the aggregation, buffering the volume change, preserving the integrity of NPs, as well as serving as the conducting matrix possibly accounts for superior electrochemical performance of the composite electrode with respect to pristine metal oxide. We expect this protocol will open up a new pathway for the realization of various graphene-based hybrid materials for diverse applications.

Acknowledgements

This work is supported by the Singapore National Research Foundation under NRF RF Award No. NRF-RF2010-07 and MOE Tier 2 MOE 2009-T2-1-037.

Notes and references

1 (*a*) C. W. Cheng, B. Liu, H. Y. Yang, W. W. Zhou, L. Sun, R. Chen, S. F. Yu, J. X. Zhang, H. Gong, H. D. Sun and H. J. Fan, *ACS Nano*, 2009, **3**, 3069–3076; (*b*) J. Liu, J. Jiang, C. Cheng, H. Li, J. Zhang, H. Gong and H. J. Fan, *Adv. Mater.*, 2011, **23**, 2076–2081; (*c*) W. Zhou, C. Cheng, J. Liu, Y. Y. Tay, J. Jiang, X. Jia, J. Zhang, H. Gong, H. H. Hng, T. Yu and H. J. Fan, *Adv. Funct. Mater.*, 2011, **21**, 2439–2446; (*d*) J. Liu, C. Cheng, W. Zhou, H. Li and H. J. Fan, *Chem. Commun.*, 2011, **47**, 3436–3438.
2 Y. H. Wu, T. Yu and Z. X. Shen, *J. Appl. Phys.*, 2010, **108**, 071301.
3 (*a*) T. H. Han, W. J. Lee, D. H. Lee, J. E. Kim, E.-Y. Choi and S. O. Kim, *Adv. Mater.*, 2010, **22**, 2060–2064; (*b*) H. Bai, C. Li and

G. Shi, *Adv. Mater.*, 2011, **23**, 1089–1115; (*c*) J. Liu, S. Fu, B. Yuan, Y. Li and Z. Deng, *J. Am. Chem. Soc.*, 2010, **132**, 7279–7281; (*d*) D. H. Lee, J. E. Kim, T. H. Han, J. W. Hwang, S. Jeon, S. Y. Choi, S. H. Hong, W. J. Lee, R. S. Ruoff and S. O. Kim, *Adv. Mater.*, 2010, **22**, 1247–1252; (*e*) S. H. Lee, D. H. Lee, W. J. Lee and S. O. Kim, *Adv. Funct. Mater.*, 2011, **21**, 1338–1354.

4 (*a*) X. H. Li, J. S. Chen, X. C. Wang, J. H. Sun and M. Antonietti, *J. Am. Chem. Soc.*, 2011, **133**, 8074–8077; (*b*) C. Peng, B. W. Jiang, Q. Liu, Z. Guo, Z. J. Xu, Q. Huang, H. J. Xu, R. Z. Tai and C. H. Fan, *Energy Environ. Sci.*, 2011, **4**, 2035–2040.

5 H. Vedala, D. C. Sorescu, G. P. Kotchey and A. Star, *Nano Lett.*, 2011, **11**, 2342–2347.

6 H. L. Li, S. P. Pang, S. Wu, X. L. Feng, K. Mullen and C. Bubeck, *J. Am. Chem. Soc.*, 2011, **133**, 9423–9429.

7 (*a*) N. Li, G. Liu, C. Zhen, F. Li, L. L. Zhang and H. M. Cheng, *Adv. Funct. Mater.*, 2011, **21**, 1717–1722; (*b*) Y. C. Qiu, K. Y. Yan, S. H. Yang, L. M. Jin, H. Deng and W. S. Li, *ACS Nano*, 2010, **4**, 6515–6526; (*c*) T. Q. Lin, F. Q. Huang, J. Liang and Y. X. Wang, *Energy Environ. Sci.*, 2011, **4**, 862–865; (*d*) K. P. Acharya, R. S. Khnayzer, T. O'Connor, G. Diederich, M. Kirsanova, A. Klinkova, D. Roth, E. Kinder, M. Imboden and M. Zamkov, *Nano Lett.*, 2011, **11**, 2919–2926; (*e*) W. W. Zhou, J. P. Liu, T. Chen, K. S. Tan, X. T. Jia, Z. Q. Luo, C. X. Chun, H. P. Yang, C. M. Li and T. Yu, *Phys. Chem. Chem. Phys.*, 2011, **13**, 14462–14465.

8 (*a*) D. Wang, D. Choi, J. Li, Z. Yang, Z. Nie, R. Kou, D. Hu, C. Wang, L. V. Saraf, J. Zhang, I. A. Aksay and J. Liu, *ACS Nano*, 2009, **3**, 907–914; (*b*) X. Zhu, Y. Zhu, S. Murali, M. D. Stoller and R. S. Ruoff, *ACS Nano*, 2011, **5**, 3333–3338; (*c*) X. Y. Wang, X. F. Zhou, K. Yao, J. G. Zhang and Z. P. Liu, *Carbon*, 2011, **49**, 133–139; (*d*) S. Ding, J. S. Chen, D. Luan, F. Y. C. Boey, S. Madhavi and X. W. Lou, *Chem. Commun.*, 2011, **47**, 5780–5782.

9 (*a*) S.-M. Paek, E. Yoo and I. Honma, *Nano Lett.*, 2008, **9**, 72–75; (*b*) Y. J. Mai, X. L. Wang, J. Y. Xiang, Y. Q. Qiao, D. Zhang, C. D. Gu and J. P. Tu, *Electrochim. Acta*, 2011, **56**, 2306–2311; (*c*) S. B. Yang, X. L. Feng, S. Ivanovici and K. Mullen, *Angew. Chem., Int. Ed.*, 2010, **49**, 8408–8411.

10 G. M. Zhou, D. W. Wang, F. Li, L. L. Zhang, N. Li, Z. S. Wu, L. Wen, G. Q. Lu and H. M. Cheng, *Chem. Mater.*, 2010, **22**, 5306–5313.

11 (*a*) Z. S. Wu, D. W. Wang, W. Ren, J. Zhao, G. Zhou, F. Li and H. M. Cheng, *Adv. Funct. Mater.*, 2010, **20**, 3595–3602; (*b*) J. X. Zhu, T. Zhu, X. Z. Zhou, Y. Y. Zhang, X. W. Lou, X. D. Chen, H. Zhang, H. H. Hng and Q. Y. Yan, *Nanoscale*, 2011, **3**, 1084–1089.

12 (*a*) Z. S. Wu, W. C. Ren, D. W. Wang, F. Li, B. L. Liu and H. M. Cheng, *ACS Nano*, 2010, **4**, 5835–5842; (*b*) W. T. Zheng, Y. M. Ho, H. W. Tian, M. Wen, J. L. Qi and Y. A. Li, *J. Phys. Chem. C*, 2009, **113**, 9164–9168; (*c*) J. O. Hwang, D. H. Lee, J. Y. Kim, T. H. Han, B. H. Kim, M. Park, K. No and S. O. Kim, *J. Mater. Chem.*, 2011, **21**, 3432–3437.

13 W. S. Hummers and R. E. Offeman, *J. Am. Chem. Soc.*, 1958, **80**, 1339.

14 (*a*) T. Yu, X. Zhao, Z. X. Shen, Y. H. Wu and W. H. Su, *J. Cryst. Growth*, 2004, **268**, 590–595; (*b*) Y. W. Zhu, T. Yu, F. C. Cheong, X. J. Xui, C. T. Lim, V. B. C. Tan, J. T. L. Thong and C. H. Sow, *Nanotechnology*, 2005, **16**, 88–92; (*c*) T. Yu, Y. W. Zhu, X. J. Xu, K. S. Yeong, Z. X. Shen, P. Chen, C. T. Lim, J. T. L. Thong and C. H. Sow, *Small*, 2006, **2**, 80–84.

15 J. Jiang, J. P. Liu, R. M. Ding, X. X. Ji, Y. Y. Hu, X. Li, A. Z. Hu, F. Wu, Z. H. Zhu and X. T. Huang, *J. Phys. Chem. C*, 2010, **114**, 929–932.

16 (*a*) S. Park, D. A. Dikin, S. T. Nguyen and R. S. Ruoff, *J. Phys. Chem. C*, 2009, **113**, 15801–15804; (*b*) J. Oh, J. H. Lee, J. C. Koo, H. R. Choi, Y. Lee, T. Kim, N. D. Luong and J. D. Nam, *J. Mater. Chem.*, 2010, **20**, 9200–9204.

17 S. Stankovich, D. A. Dikin, G. H. B. Dommett, K. M. Kohlhaas, E. J. Zimney, E. A. Stach, R. D. Piner, S. T. Nguyen and R. S. Ruoff, *Nature*, 2006, **442**, 282–286.

18 J. Z. Wang, C. Zhong, D. Wexler, N. H. Idris, Z. X. Wang, L. Q. Chen and H. K. Liu, *Chem.–Eur. J.*, 2011, **17**, 661–667.

19 (*a*) J. P. Liu, Y. Y. Li, H. J. Fan, Z. H. Zhu, J. Jiang, R. M. Ding, Y. Y. Hu and X. T. Huang, *Chem. Mater.*, 2010, **22**, 212–217; (*b*) M. V. Reddy, T. Yu, C. H. Sow, Z. X. Shen, C. T. Lim, G. V. S. Rao and B. V. R. Chowdari, *Adv. Funct. Mater.*, 2007, **17**, 2792–2799.

20 X. L. Wu, Y. G. Guo, L. J. Wan and C. W. Hu, *J. Phys. Chem. C*, 2008, **112**, 16824–16829.

21 (*a*) Y. X. Chen, L. H. He, P. J. Shang, Q. L. Tang, Z. Q. Liu, H. B. Liu and L. P. Zhou, *J. Mater. Sci. Technol.*, 2011, **27**, 41–45; (*b*) L. Q. Mai, B. Hu, W. Chen, Y. Y. Qi, C. S. Lao, R. S. Yang, Y. Dai and Z. L. Wang, *Adv. Mater.*, 2007, **19**, 3712–3716; (*c*) J. S. Chen, Y. L. Cheah, S. Madhavi and X. W. Lou, *J. Phys. Chem. C*, 2010, **114**, 8675–8678.